

Kibble-Zurek mechanism for dissipative discrete time crystals

Roy D. Jara Jr.* and Jayson G. Cosme†

National Institute of Physics, University of the Philippines, Diliman, Quezon City 1101, Philippines

We demonstrate that the Kibble-Zurek mechanism (KZM) holds for open systems transitioning from a disordered phase to a discrete time crystal (DTC). Specifically, we observe the main signatures of the KZM when the system is quenched into a DTC, which are the characteristic power-law scaling with quench time of the number of spatial defects and the transition delay measured from the time at which the system crosses the critical point. We show analytically that this universal behavior can be traced back to how systems that can be mapped onto a dissipative linear parametric oscillator (DLPO) satisfy the adiabatic-impulse (AI) approximation, evinced by the divergence of the relaxation time of the DLPO near a critical point. We verify our predictions in both the classical and quantum regimes by considering two systems: the Sine-Gordon model, which is a paradigmatic system for emulating classical DTCs; and the open Dicke lattice model, an array of spin-boson systems subjected to quantum fluctuations. For both systems, the DTCs can be tuned from a ferromagnetic to an antiferromagnetic order by varying the driving frequency, thus allowing us to test the validity of KZM for arbitrary spatiotemporal ordering.

The KZM is a well-celebrated theory in understanding the universal behavior of quenched systems. It relates the formation of defects on a system transitioning from a disordered to an ordered phase to the speed at which a critical point is crossed. The KZM predicts that the number of defects n_d that form after the quench follows an inverse power-law relationship with the quench timescale τ_q , with the scaling set by the critical exponents of the system's universality class [1]. The KZM has been tested across multiple platforms, ranging from closed systems [2–15] to driven [16–23], and open systems [24–31].

Despite its success in explaining the proliferation of defects in quenched systems, the KZM has so far only been applied in systems undergoing a transition towards a spatially ordered phase that remains static in the long-time limit. Thus, the question remains whether the KZM also applies to systems undergoing a spatiotemporal ordering, for instance, in DTCs. A DTC is a dynamical phase that emerges as the discrete time-translation symmetry imposed by an external periodic drive is spontaneously broken in a many-body system [32, 33]. It is characterized by subharmonic oscillation of observables with a period slower than the drive, wherein the most fundamental example is period-doubled DTCs [32, 33]. The DTCs have been extensively studied and observed experimentally across multiple platforms, ranging from, but not limited to, networks of classical oscillators [34–38], spin systems [39–47], bosonic systems [48–55], superconductors [56–58], and particles under oscillating mediums [59–61].

While it has been shown that DTCs can exhibit critical behaviors reminiscent of those observed in equilibrium systems, such as the divergence of the relaxation time [38, 45, 46] and fluctuations [38], it remains to be seen whether a quench leading to the formation of a DTC exhibits universal behaviors. In this Letter, we demonstrate that the KZM holds for open systems transitioning from a disordered to a spatiotemporally ordered phase.

To this end, we show that the AI approximation, which is the cornerstone of the KZM, applies to DLPO. As such, if a system with dimension $D \geq 1$ can be mapped onto a DLPO, then it can exhibit the main signatures of the KZM following a quench that results to a DTC. These signatures are the power law scaling with τ_q of the defect number and the transition delay from the time the system crosses the critical point. We first test this prediction on the Sine-Gordon model (SGM), which is a paradigmatic model for studying classical DTCs [35]. We then consider the open Dicke lattice model (DLM) that describes a lattice of spin-boson systems subject to quantum fluctuations due to cavity dissipation [62]. By considering these two systems, we verify the universality of the KZM on temporally ordered phases both in the classical and quantum regimes.

AI approximation for DTCs – Let us begin with a brief review of the AI approximation and how the KZM emerges as a result. Consider a generic system that can undergo a continuous phase transition from a disordered to an ordered phase by tuning a control parameter A across some critical point A_c . Near the critical point, the system's relaxation time τ and correlation length ξ diverges, with $\tau \propto |\varepsilon|^{-vz}$ and $\xi \propto |\varepsilon|^{-v}$, where $\varepsilon = (A - A_c)/A_c$ [1]. Here, v and z are the static and dynamic critical exponents respectively. Suppose we linearly ramp A using the protocol,

$$A(t) = \begin{cases} A_i & t_i \leq t \leq 0 \\ (A_f - A_i) \left(\frac{t}{\tau_q} \right) + A_i, & 0 < t < \tau_q, \\ A_f & \tau_q \leq t \leq t_f, \end{cases} \quad (1)$$

where A_i and A_f are the initial and final values of the control parameter, respectively, while t_i and t_f are the initial and final time. We also initialize the system deep in the disordered phase, $A_i \ll A_c$, and assume that τ_q is sufficiently large. Initially, the system remains in an adiabatic regime where any of its macroscopic quantities

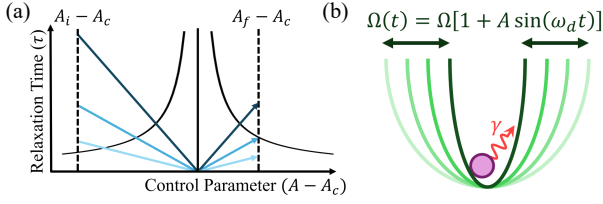


FIG. 1. (a) Sketch of the adiabatic-impulse approximation for finite ramp protocols. (b) Sketch of a generic dissipative linear parametric oscillator.

adiabatically follow the quench. As A approaches A_c , the system enters an impulse regime, in which the divergence of τ causes the system's to remain frozen in the disordered phase even after the system has passed A_c at the critical time t_c . The system only leaves the impulse regime after some transition time t_p , with $t_p > t_c$. This crossover of the system from an adiabatic dynamics to a frozen dynamics constitutes the AI approximation of the KZM [1]. A sketch of this approximation is shown in Fig. 1(a).

One of the key assumption of the KZM is that the relaxation time at $A(t_p)$ sets the transition delay $\hat{t} \equiv t_p - t_c$, with $\hat{t} \propto \tau(A(t_p))$ [1]. Meanwhile, the correlation length at t_p , $\xi(t_p)$, sets the number of defects in the system's spatial configuration post-quench. Specifically, n_d follows the relation $n_d \propto \xi(t_p)^{-(D-d)}$, where D is the system's dimension, and d is the defect dimension [1]. These two assumptions lead to the main signatures of the KZM: the power-law scaling of n_d and \hat{t} with τ_q ,

$$\hat{t} \propto \tau_q^{\frac{vz}{1+vz}}, \quad n_d \propto \tau_q^{-(D-d)\frac{v}{1+vz}}. \quad (2)$$

Showing that a quenched system exhibits these scaling behaviors is enough to demonstrate that the system follows the KZM [1]. Note that for a finite ramp protocol, the KZM is expected to break down at very small values of τ_q , resulting in a constant \hat{t} and n_d [29, 30].

Now, to show that an open system undergoing a transformation into a DTC can exhibit signatures of the KZM, we have to first demonstrate that it satisfies the condition for the AI approximation. This condition is the divergence of the relaxation time near the critical point. To do this, consider a DLPO

$$\ddot{\theta} + \gamma\dot{\theta} + \Omega^2 [1 + A \sin(\omega_d t)] \theta = 0, \quad (3)$$

where γ is the dissipation rate, Ω is the natural frequency, and ω_d and A are the driving frequency and amplitude, respectively. A generic sketch of this system is shown in Fig. 1(b). As shown in Refs. [63, 64], a huge class of systems that can form DTCs can be mapped onto a DLPO. When driven resonantly at $\omega_d = 2\Omega$, the DLPO has two states, a disordered state represented by $\theta \approx 0$ and a resonant state where θ exponential grows in time as it oscillates with a period twice the driving period

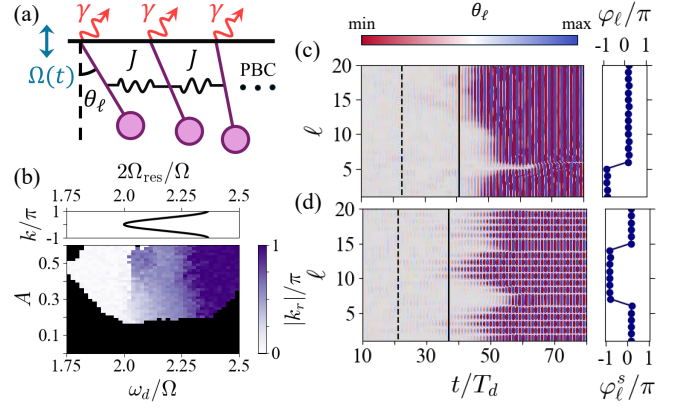


FIG. 2. (a) Sketch of the Sine-Gordon model. (b) Top panel shows the dispersion relation of the SGM, while the bottom panel shows the phase diagram of the SGM as a function of ω_d and A for $\gamma = 0.1\Omega$, $g = 0.1\Omega^2$ and $\tilde{T} = 10^{-5}$. (c)–(d) (Left panel) Exemplary spatiotemporal dynamics of θ_ℓ for (c) FM-DTC, $\omega_d = 1.9\Omega$, and (d) AFM-DTC $\omega_d = 2.4\Omega$, with quench time $\tau_q/T_d = 50$. The dashed lines correspond to the critical time t_c while the solid lines mark the transition time t_p . (Right panel) Exemplary defect configuration associated with the (c) FM-DTC and (d) AFM-DTC shown in the right panel.

T_d . These two states are separated by a critical driving amplitude $A_c = 2\gamma/\Omega$. Now, near A_c for $A < A_c$, the system is in the disordered state with $\theta \approx \alpha(t)e^{i\omega_d t/2} + cc.$, where $\alpha(t) = \alpha_0 e^{-\omega_d t/\tau}$ is the response amplitude, and α_0 is a constant set by the initial state [64]. Here, $\tau \propto (A - A_c)^{-1}$ is the relaxation time of the response amplitude. Notably, τ diverges as $A \rightarrow A_c$, satisfying the condition for the AI approximation. Following this, if we can show that a system with dimension $D \geq 1$ can be mapped onto a DLPO, then the AI approximation must hold for the system when quenched to form a DTC, thereby exhibiting the signatures of the KZM.

KZM for Classical DTCs – Let us now demonstrate that the KZM holds for classical DTCs. For this, consider the SGM, which is an array of M coupled pendula as shown in Fig. 2(a). It is described by the equation

$$\ddot{\theta}_\ell + \gamma\dot{\theta}_\ell + f(t) \sin \theta_\ell - g(\theta_{\ell-1} + \theta_{\ell+1} - 2\theta_\ell) = \eta_\ell, \quad (4)$$

where g is the nearest-neighbor coupling strength, and $f(t) = \Omega^2 [1 + A(t) \sin(\omega_d t)]$ is the periodic driving. The Gaussian white noise η_ℓ represents the thermal bath connected to each pendulum. It satisfies the relation $\langle \eta_\ell(t) \rangle = 0$ and $\langle \eta_\ell(t) \eta_{\ell'}(t') \rangle = 2\tilde{T}\Omega^2 \gamma \delta(t-t') \delta_{\ell,\ell'}$, where $\tilde{T} = k_B T / (mL^2\Omega^2)$ is the unitless temperature [35]. Here, m and L are the characteristic mass and length of each pendulum, respectively, and k_B is the Boltzmann constant.

In the small temperature limit, $\tilde{T} \ll 1$ and $A(t) = A$, a classical DTC may emerge in the SGM by driving the system at a frequency near the twice of its natural fre-

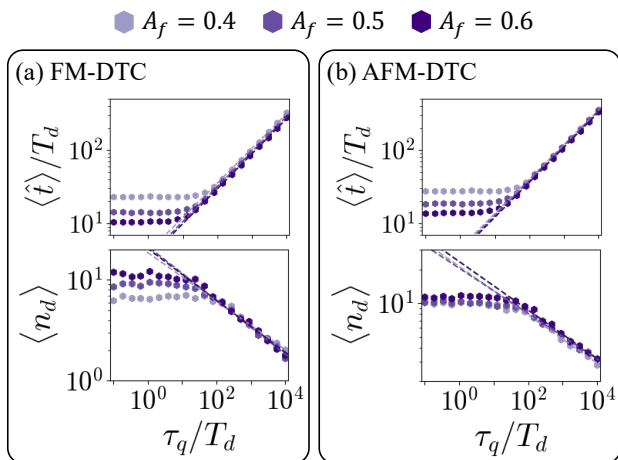


FIG. 3. (a)–(b) KZM scaling of the SGM for (a) the FM-DTC, $\omega_d = 1.9\Omega$, and (b) the AFM-DTC, $\omega_d = 2.4\Omega$, with the parameters $\gamma = 0.1\Omega$, $g = 0.1\Omega^2$, $\tilde{T} = 10^{-5}$, and $M = 100$ sites. The top panels show the scaling of the average transition delay $\langle \hat{t} \rangle$, while the bottom panels show the scaling of the average defect number $\langle n_d \rangle$ in the long time limit. The dashed lines correspond to the best-fit line for $\langle \hat{t} \rangle$ and $\langle n_d \rangle$, respectively.

quency band $\Omega_{\text{res}}(k)$. We show $\Omega_{\text{res}}(k)$ in the top panel of Fig. 2(b), while we present in the bottom panel the phase diagram of the SGM as a function A and ω_d for the parameters $\gamma = 0.1\Omega$, $g = 0.1\Omega^2$, and $\tilde{T} = 10^{-5}$. As seen in Fig. 2(b), depending on the value of ω_d , we can excite classical DTCs with spatial modulation at a quasimomentum k_r . In particular, if $\omega_d \leq 2\Omega_{\text{res}}(k=0)$, we can excite a ferromagnetic DTC (FM-DTC), in which its response amplitude is homogeneous across all space, i.e., $|k_r| = 0$. We show an exemplary dynamics of this in Fig. 2(c). Meanwhile, if $\omega_d \geq 2\Omega_{\text{res}}(k=\pi)$, we can excite an antiferromagnetic DTC (AFM-DTC), in which the oscillation phase shift alternates every other site and $|k_r| = \pi$. An exemplary dynamics for this configuration is shown in Fig. 2(d). This tunability of the spatial configuration of the classical DTCs in the SGM allows us to test the KZM for arbitrary spatiotemporal order.

We now provide a general recipe for testing the KZM in any lattice system transitioning into a DTC. Consider a local order parameter $O_\ell(t)$ exhibiting period-doubling oscillations in the DTC phase. To obtain \hat{t} and n_d , the fast oscillating terms of $O_\ell(t)$ can be integrated out to obtain the complex amplitude [65, 66]

$$O_{\ell,R}(t) = \frac{\omega_R}{\pi} \int_t^{t+2\pi/\omega_R} O_\ell(t') e^{i\omega_R t'} dt', \quad (5)$$

where $\omega_R = \omega_d/2$ is the dominant frequency of O_ℓ in the DTC phase. Here, $|O_{\ell,R}|$ captures the response amplitude of O_ℓ , while $\varphi_\ell \equiv \arg \{O_{\ell,R}\}$ captures the oscillation phase shift. In a DTC, φ_ℓ can only have two values corresponding to the two degenerate symmetry-broken

states of a DTC [66], making it an ideal quantity for identifying defects. We determine t_p using a threshold criterion, in which we identify the existence of a DTC when $\sum_\ell |O_{\ell,R}| \geq \delta \max \{\sum_\ell |O_{\ell,R}|\}$, with $\delta = 0.15$. For t_c , we use the relation $t_c = (A_c - A_i) \tau_q / (A_f - A_i)$ inferred from Eq. (1). Here, we obtain A_c by considering the scaling of $A(t_p)$ with τ_q and extrapolating its value as $\tau_q \rightarrow \infty$ (see [64] for details). Finally, to determine n_d , we consider φ_ℓ as the main order parameter for identifying defects in FM-DTCs. Meanwhile, we use the staggered phase $\varphi_\ell^s = \varphi_\ell + [1 - (-1)^\ell] \pi/2$, with $\varphi_\ell^s \in [-\pi, \pi]$, for identifying defects in the AFM-DTC. An exemplary spatial profile of φ_ℓ and φ_ℓ^s is shown in the right panels of Fig. 2(c) and 2(d), respectively, for $O_\ell = \theta_\ell$.

We now present in the top panels of Figs. 3(a) and 3(b) the average transition delay $\langle \hat{t} \rangle \equiv \langle t_p \rangle - t_c$ of the SGM as a function of τ_q for the FM-DTC and the AFM-DTC, respectively. The ramp protocol used here is given by Eq. (1), with $A_i = 0$. We then show in the bottom panels of Figs. 3(a) and 3(b) the average defect number $\langle n_d \rangle$ for the FM-DTC and AFM-DTC, respectively. Here, $O_\ell = \theta_\ell$ and we perform an ensemble average of \hat{t} and n_d for 100 noise realizations. For both DTC configurations, $\langle \hat{t} \rangle$ and $\langle n_d \rangle$ follow a power-law scaling with τ_q above $\tau_q/T_d = 10^2$. This behavior signifies that the KZM indeed holds when DTCs form in classical open systems. Below $\tau_q/T_d = 10^2$, $\langle \hat{t} \rangle$ and $\langle n_d \rangle$ saturate at a finite value, indicating the breakdown of KZM at small τ_q , which is a universal feature of systems under finite-quench protocols [29, 30].

KZM in Quantum DTCs – Now that we have shown that the KZM holds for classical DTCs, we next explore whether this mechanism still holds in the quantum regime. For this, we consider the DLM, which is described by the Lindblad master equation [62]

$$\partial_t \hat{\rho} = i \left[\hat{H}/\hbar, \hat{\rho} \right] + \kappa \sum_{\ell=1}^M \left(2\hat{a}_\ell \hat{\rho} \hat{a}_\ell^\dagger - \left\{ \hat{a}_\ell^\dagger \hat{a}_\ell, \hat{\rho} \right\} \right), \quad (6)$$

where $\hat{H} = \sum_{\ell=1}^M \hat{H}_\ell$ and

$$\frac{\hat{H}_\ell}{\hbar} = \omega \hat{a}_\ell^\dagger \hat{a}_\ell + \omega_0 \hat{S}_\ell^z + \frac{2\lambda}{\sqrt{N}} \left(\hat{a}_\ell^\dagger + \hat{a}_\ell \right) \hat{S}_\ell^x - J \left(\hat{a}_\ell^\dagger \hat{a}_{\ell+1} + \text{hc.} \right). \quad (7)$$

The DLM, schematically depicted in Fig. 4(a), describes the dynamics of $M \cdot N$ two-level systems equally partitioned into M lattice sites. Each site is coupled to a single lossy bosonic mode, represented by the annihilation operator \hat{a}_ℓ . The two-level systems in each site are represented by the collective spin operator $\hat{S}_\ell^{x,y,z}$. Here, ω and ω_0 are the boson and spin transition frequencies, respectively, and J is the nearest-neighbor coupling of the bosonic modes. The spin-boson coupling λ is periodically driven such that $\lambda(t) = \lambda_0 [1 + A(t) \sin(\omega_d t)]$. Throughout the remainder of this work, we set $\omega = \omega_0$, and we employ the truncated Wigner approximation to obtain

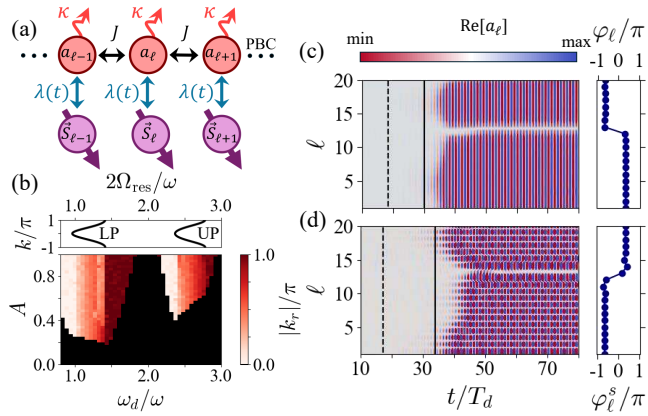


FIG. 4. (a) Sketch of the open Dicke lattice model. (b) Top panel shows the polariton bands of the DLM, $\Omega_{\text{res,LP}}(k)$ and $\Omega_{\text{res,UP}}(k)$, while the bottom panel shows the phase diagram of the DLM as a function of A and ω_d for $\lambda_0 = 0.7\lambda_c$, $\kappa = J = 0.1\omega$, and $N = 10^4$. (c)–(d) (Left panel) Exemplary spatiotemporal dynamics of the DLM for (a) the FM-DTC, $\omega_d = 0.9\omega$ and (b) the AFM-DTC, $\omega_d = 1.5\omega$, with quench time $\tau_q/T_d = 50$. The dashed lines correspond to t_c , while the solid lines mark t_p . (Right panel) Exemplary defect configuration associated with (c) the FM-DTC and (d) the AFM-DTC shown in the left panel.

the system’s dynamics. This approximation allows us to incorporate the first-order correction to the quantum fluctuations without solving the full density matrix of the system, which exponentially grows with system size [67]. The full details of the approximation are given in [64].

For nonzero dissipation rate, $\kappa \ll \omega$, and $J \ll |\omega - \kappa|/2$, the DLM is known to have two static phases. Below the critical point $\lambda_c = \frac{1}{2}\sqrt{\omega[(\omega - 2J)^2 + \kappa^2]}/(\omega - 2J)$, the system is in the normal phase, which is characterized by zero photon number $|a_{\ell}|^2 \equiv \langle a_{\ell}^{\dagger} a_{\ell} \rangle$ and fully-polarized $S_{\ell}^z \equiv \langle \hat{S}_{\ell}^z \rangle$ in the negative z -direction [30, 62]. Above λ_c , the system breaks its \mathbb{Z}_2 symmetry, resulting to a homogeneous superradiant phase. It is characterized by a nonzero $|a_{\ell}|^2$ and a nonzero component for $S_{\ell}^x \equiv \langle \hat{S}_{\ell}^x \rangle$. The value of S_{ℓ}^x is dependent on the configuration set by the system’s correlation length after a transition from the normal phase [30, 62].

Similar to the SGM, for $\lambda_0 < \lambda_c$ and $A(t) = A$, we can also induce a spatiotemporal order in the DLM by periodically driving $\lambda(t)$ near the twice its lower and upper polariton bands, $\Omega_{\text{res,LP}}(k)$ and $\Omega_{\text{res,UP}}(k)$, respectively. The polariton bands are shown in the top panel of Fig. 4(b), while the resulting phase diagram is shown in the bottom panel of Fig. 4(b) for the parameters $\lambda_0 = 0.7\lambda_c$, $\kappa = J = 0.1\omega$, and $N = 10^4$. Focusing on the resonance tongue associated with $\Omega_{\text{res,LP}}(k)$, we see that we can also excite an FM-DTC by driving at $\omega_d \leq 2\Omega_{\text{res,LP}}(k = 0)$, while we can excite an AFM-DTC by driving at $\omega_d \geq 2\Omega_{\text{res,LP}}(k = \pi)$. Their respective ex-

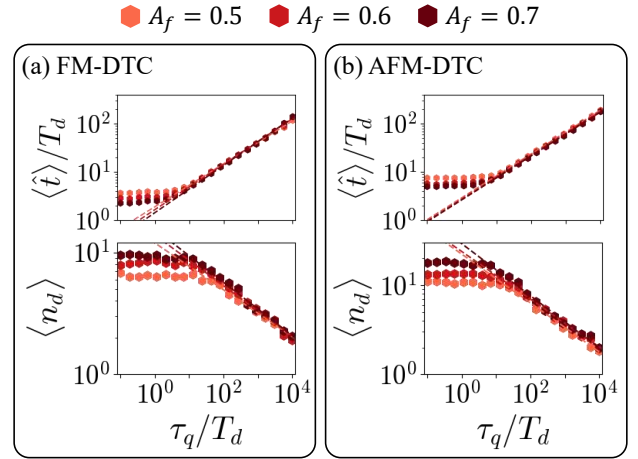


FIG. 5. (a)–(b) KZM scaling of the DLM for (a) the FM-DTC, $\omega_d = 0.9\omega$, and (b) the AFM-DTC, ω_d , with the parameters $\lambda_0 = 0.7\lambda_c$, $\kappa = J = 0.1\omega$, $N = 10^4$, and $M = 100$ sites. The top panels show the scaling of $\langle \hat{t} \rangle$ as a function of τ_q , while the bottom panels show the scaling of $\langle n_d \rangle$. The dashed lines correspond to the best fit lines for the $\langle \hat{t} \rangle$ and $\langle n_d \rangle$, respectively.

emplary dynamics are shown in Figs. 4(c) and 4(d). This allows us to also test the KZM for both the FM-DTCs and AFM-DTCs of the DLM.

We now test whether the KZM still holds for DTCs subject to quantum noise by using Eq. (1) to quench the DLM towards a DTC from $A_i = 0$. For this, we consider $O_{\ell} = a_{\ell}$, where $a_{\ell} \in \mathbb{C}$ is a single noise realization of the bosonic mode at site ℓ [64]. We then use the same recipe employed in the SGM to obtain \hat{t} and n_d . We present in Figs. 5(a) and 5(b) the scaling of $\langle \hat{t} \rangle$ and $\langle n_d \rangle$ for the FM-DTC and AFM-DTC of the DLM, respectively. The ensemble average is performed over 100 noise realizations. Similar to the SGM, we observe a power-law scaling of $\langle \hat{t} \rangle$ and $\langle n_d \rangle$ at $\tau_q/T_d \geq 10$, which is a clear signature of the KZM. Below this quench time, we observe the breakdown of the KZM, which, again, is a universal feature of finite quenches [29, 30].

Conclusion—We have demonstrated that the KZM holds for open systems transitioning from a disordered phase to a spatiotemporally ordered phase both in the classical and quantum regime. This shows that the universal behavior of quenched open systems extends even for ordered phases in which the system remains dynamic indefinitely, such as in time crystals. Our results can be tested in platforms that can emulate an array of parametric oscillators [34, 37, 68–70], and array of spin-boson systems [62, 71–75].

Acknowledgement—R.D.J. acknowledges support from the DOST-SEI under the Accelerated Science and Technology Human Resource Development Program. J.G.C. acknowledges financial support from National Academy of Science and Technology, Philippines (NAST PHL). We

thank P. Kongkhambut, H. Keßler, and A. Hemmerich for insightful discussions.

* rjara@nip.upd.edu.ph

† jcosme@nip.upd.edu.ph

- [1] A. del Campo and W. H. Zurek, Universality of Phase Transition Dynamics: Topological Defects from Symmetry Breaking, *Int. J. Mod. Phys. A* **29**, 1430018 (2014).
- [2] Q. Ye, S. Wu, X. Jiang, and C. Lee, Universal dynamics of zero-momentum to plane-wave transition in spin-orbit coupled Bose-Einstein condensates, *J. Stat. Mech.* **2018**, 053110 (2018).
- [3] I. Kang Liu, J. Dziarmaga, S.-C. Gou, F. Dalfovo, and N. P. Proukakis, Kibble-Zurek Dynamics in a Trapped Ultracold Bose Gas, *Phys. Rev. Research* **2**, 033183 (2020).
- [4] N. Navon, A. L. Gaunt, R. P. Smith, and Z. Hadzibabic, Critical Dynamics of Spontaneous Symmetry Breaking in a Homogeneous Bose gas, *Science* **347**, 167 (2015).
- [5] D. Nagy, G. Szirmai, and P. Domokos, Self-organization of a Bose-Einstein condensate in an optical cavity, *Eur. Phys. J. D* **48**, 127 (2008).
- [6] K. Shimizu, Y. Kuno, T. Hirano, and I. Ichinose, Dynamics of a quantum phase transition in the Bose-Hubbard model: Kibble-Zurek mechanism and beyond, *Phys. Rev. A* **97**, 033626 (2018).
- [7] J. Dziarmaga and J. M. Mazur, Tensor network simulation of the quantum Kibble-Zurek quench from the Mott to the superfluid phase in the two-dimensional Bose-Hubbard model, *Phys. Rev. B* **107**, 144510 (2023).
- [8] M. Anquez, B. Robbins, H. Bharath, M. Boguslawski, T. Hoang, and M. Chapman, Quantum Kibble-Zurek Mechanism in a Spin-1 Bose-Einstein Condensate, *Phys. Rev. Lett.* **116**, 155301 (2016).
- [9] M. Schmitt, M. M. Rams, J. Dziarmaga, M. Heyl, and W. H. Zurek, Quantum phase transition dynamics in the two-dimensional transverse-field Ising model, *Sci. Adv.* **8**, eabl6850 (2022).
- [10] B.-W. Li, Y.-K. Wu, Q.-X. Mei, R. Yao, W.-Q. Lian, M.-L. Cai, Y. Wang, B.-X. Qi, L. Yao, L. He, Z.-C. Zhou, and L.-M. Duan, Probing Critical Behavior of Long-Range Transverse-Field Ising Model through Quantum Kibble-Zurek Mechanism, *PRX Quantum* **4**, 010302 (2023).
- [11] K. Du, X. Fang, C. Won, C. De, F.-T. Huang, W. Xu, H. You, F. J. Gómez-Ruiz, A. del Campo, and S.-W. Cheong, Kibble-Zurek mechanism of Ising domains, *Nat. Phys.* **10.1038/s41567-023-02112-5** (2023).
- [12] A. Keesling, A. Omran, H. Levine, H. Bernien, H. Pichler, S. Choi, R. Samajdar, S. Schwartz, P. Silvi, S. Sachdev, P. Zoller, M. Endres, M. Greiner, V. Vuletić, and M. D. Lukin, Quantum Kibble-Zurek mechanism and critical dynamics on a programmable Rydberg simulator, *Nature* **568**, 207 (2019).
- [13] N. Chepiga and F. Mila, Kibble-Zurek exponent and chiral transition of the period-4 phase of Rydberg chains, *Nat Commun* **12**, 414 (2021).
- [14] J.-M. Cui, Y.-F. Huang, Z. Wang, D.-Y. Cao, J. Wang, W.-M. Lv, L. Luo, A. del Campo, Y.-J. Han, C.-F. Li, and G.-C. Guo, Experimental Trapped-ion Quantum Simulation of the Kibble-Zurek dynamics in momentum space, *Sci Rep* **6**, 33381 (2016).
- [15] S. Ulm, J. Roßnagel, G. Jacob, C. Degünther, S. T. Dawkins, U. G. Poschinger, R. Nigmatullin, A. Retzker, M. B. Plenio, F. Schmidt-Kaler, and K. Singer, Observation of the Kibble-Zurek scaling law for defect formation in ion crystals, *Nat Commun* **4**, 2290 (2013).
- [16] C. J. O. Reichhardt, A. del Campo, and C. Reichhardt, Kibble-Zurek mechanism for nonequilibrium phase transitions in driven systems with quenched disorder, *Commun Phys* **5**, 1 (2022).
- [17] S. Maegochi, K. Ienaga, and S. Okuma, Kibble-Zurek Mechanism for Dynamical Ordering in a Driven Vortex System, *Phys. Rev. Lett.* **129**, 227001 (2022).
- [18] W.-C. Yang, M. Tsubota, A. del Campo, and H.-B. Zeng, Universal defect density scaling in an oscillating dynamic phase transition, *Phys. Rev. B* **108**, 174518 (2023).
- [19] L. W. Clark, L. Feng, and C. Chin, Universal space-time scaling symmetry in the dynamics of bosons across a quantum phase transition, *Science* **354**, 606 (2016).
- [20] A. Russomanno and E. G. D. Torre, Kibble-Zurek scaling in periodically driven quantum systems, *EPL* **115**, 30006 (2016).
- [21] B. M. Anderson, L. W. Clark, J. Crawford, A. Glatz, I. S. Aranson, P. Scherpelz, L. Feng, C. Chin, and K. Levin, Direct lattice shaking of Bose condensates: Finite momentum superfluids, *Phys. Rev. Lett.* **118**, 220401 (2017).
- [22] S. Zamani, J. Naji, R. Jafari, and A. Langari, Scaling and universality at ramped quench dynamical quantum phase transitions, *J. Phys.: Condens. Matter* **36**, 355401 (2024).
- [23] W. Verstraelen and M. Wouters, Classical critical dynamics in quadratically driven Kerr resonators, *Phys. Rev. A* **101**, 043826 (2020).
- [24] D. Rossini and E. Vicari, Dynamic Kibble-Zurek scaling framework for open dissipative many-body systems crossing quantum transitions, *Phys. Rev. Research* **2**, 023211 (2020).
- [25] A. Zamora, G. Dagvadorj, P. Comaron, I. Carusotto, N. P. Proukakis, and M. H. Szymanska, Kibble-Zurek mechanism in driven-dissipative systems crossing a nonequilibrium phase transition, *Phys. Rev. Lett.* **125**, 095301 (2020).
- [26] R. Puebla, A. Smirne, S. F. Huelga, and M. B. Plenio, Universal Anti-Kibble-Zurek Scaling in Fully Connected Systems, *Phys. Rev. Lett.* **124**, 230602 (2020).
- [27] A. Bácsi and B. Dóra, Kibble-Zurek scaling due to environment temperature quench in the transverse field Ising model, *Sci. Rep.* **13**, 4034 (2023).
- [28] J. Klinder, H. Keßler, M. Wolke, L. Mathey, and A. Hemmerich, Dynamical phase transition in the open Dicke model, *Proc Natl Acad Sci USA* **112**, 3290 (2015).
- [29] H.-B. Zeng, C.-Y. Xia, and A. del Campo, Universal breakdown of Kibble-Zurek scaling in fast quenches across a phase transition, *Phys. Rev. Lett.* **130**, 060402 (2023).
- [30] R. D. Jara Jr. and J. G. Cosme, Apparent delay of the Kibble-Zurek mechanism in quenched open systems, *Phys. Rev. B* **110**, 064317 (2024).
- [31] H.-C. Kou, Z.-H. Zhang, and P. Li, Kibble-Zurek scaling immune to anti-Kibble-Zurek behavior in driven open systems at the limit of loss difference, *Phys. Rev. B* **111**, 155152 (2025).
- [32] D. V. Else, C. Monroe, C. Nayak, and N. Y. Yao, Discrete

- time crystals, *Annu. Rev. Condens. Matter Phys.* **11**, 467 (2020).
- [33] M. P. Zaletel, M. Lukin, C. Monroe, C. Nayak, F. Wilczek, and N. Y. Yao, *Colloquium* : Quantum and classical discrete time crystals, *Rev. Mod. Phys.* **95**, 031001 (2023).
- [34] T. L. Heugel, M. Oscity, A. Eichler, O. Zilberberg, and R. Chitra, Classical many-body time crystals, *Phys. Rev. Lett.* **123**, 124301 (2019).
- [35] N. Y. Yao, C. Nayak, L. Balents, and M. P. Zaletel, Classical discrete time crystals, *Nat. Phys.* **16**, 438 (2020).
- [36] Z. G. Nicolaou and A. E. Motter, Anharmonic classical time crystals: A coreonance pattern formation mechanism, *Phys. Rev. Research* **3**, 023106 (2021).
- [37] T. L. Heugel, A. Eichler, R. Chitra, and O. Zilberberg, The role of fluctuations in quantum and classical time crystals, *SciPost Phys. Core* **6**, 053 (2023).
- [38] S. Yi-Thomas and J. D. Sau, Theory for dissipative time crystals in coupled parametric oscillators, *Phys. Rev. Lett.* **133**, 266601 (2024).
- [39] A. Russomanno, F. Iemini, M. Dalmonte, and R. Fazio, Floquet time crystal in the Lipkin-Meshkov-Glick model, *Phys. Rev. B* **95**, 214307 (2017).
- [40] N. Euler, A. Braemer, L. Benn, and M. Gärttner, Metronome spin stabilizes time-crystalline dynamics, *Phys. Rev. B* **109**, 224301 (2024).
- [41] A. Lazarides, S. Roy, F. Piazza, and R. Moessner, Time crystallinity in dissipative Floquet systems, *Phys. Rev. Res.* **2**, 022002 (2020).
- [42] P. Frey and S. Rachel, Realization of a discrete time crystal on 57 qubits of a quantum computer, *Science Advances* **8**, eabm7652 (2022).
- [43] D. V. Else, B. Bauer, and C. Nayak, Floquet time crystals, *Phys. Rev. Lett.* **117**, 090402 (2016).
- [44] A. Pizzi, J. Knolle, and A. Nunnenkamp, Higher-order and fractional discrete time crystals in clean long-range interacting systems, *Nat. Commun.* **12**, 2341 (2021).
- [45] K. Chinzei and T. N. Ikeda, Criticality and rigidity of dissipative discrete time crystals in solids, *Phys. Rev. Research* **4**, 023025 (2022).
- [46] W. Zhang, Y. Wu, X. Qiu, J. Nan, and X. Li, Subexponential critical slowing-down at a Floquet time-crystal phase transition, *Phys. Rev. B* **108**, 014307 (2023).
- [47] J. O'Sullivan, O. Lunt, C. W. Zollitsch, M. L. W. Thewalt, J. J. L. Morton, and A. Pal, Signatures of discrete time crystalline order in dissipative spin ensembles, *New J. Phys.* **22**, 085001 (2020).
- [48] A. Pizzi, J. Knolle, and A. Nunnenkamp, Period- n discrete time crystals and quasicrystals with ultracold bosons, *Phys. Rev. Lett.* **123**, 150601 (2019).
- [49] L. R. Bakker, M. S. Bahovadinov, D. V. Kurlov, V. Gritsev, A. K. Fedorov, and D. O. Krimer, Driven-dissipative time crystalline phases in a two-mode bosonic system with Kerr nonlinearity, *Phys. Rev. Lett.* **129**, 250401 (2022).
- [50] P. Kongkhambut, H. Keßler, J. Skulte, L. Mathey, J. G. Cosme, and A. Hemmerich, Realization of a periodically driven open three-level Dicke model, *Phys. Rev. Lett.* **127**, 253601 (2021).
- [51] J. Skulte, P. Kongkhambut, H. Keßler, A. Hemmerich, L. Mathey, and J. G. Cosme, Parametrically driven dissipative three-level Dicke model, *Phys. Rev. A* **104**, 063705 (2021).
- [52] H. Keßler, P. Kongkhambut, C. Georges, L. Mathey, J. G. Cosme, and A. Hemmerich, Observation of a dissipative time crystal, *Phys. Rev. Lett.* **127**, 043602 (2021).
- [53] R. J. L. Tuquero, J. Skulte, L. Mathey, and J. G. Cosme, Dissipative time crystal in an atom-cavity system: Influence of trap and competing interactions, *Phys. Rev. A* **105**, 043311 (2022).
- [54] J. G. Cosme, J. Skulte, and L. Mathey, Time crystals in a shaken atom-cavity system, *Phys. Rev. A* **100**, 053615 (2019).
- [55] H. Taheri, A. B. Matsko, L. Maleki, and K. Sacha, All-optical dissipative discrete time crystals, *Nat Commun* **13**, 848 (2022).
- [56] H. P. O. Collado, G. Usaj, C. A. Balseiro, D. H. Zanette, and J. Lorenzana, Dynamical phase transitions in periodically driven bardeen-cooper-schrieffer systems, *Phys. Rev. Res.* **5**, 023014 (2023).
- [57] H. P. Ojeda Collado, G. Usaj, C. A. Balseiro, D. H. Zanette, and J. Lorenzana, Emergent parametric resonances and time-crystal phases in driven Bardeen-Cooper-Schrieffer systems, *Phys. Rev. Research* **3**, L042023 (2021).
- [58] G. Homann, J. G. Cosme, and L. Mathey, Higgs time crystal in a high-Tc superconductor, *Phys. Rev. Research* **2**, 043214 (2020).
- [59] A. Kuroś, R. Mukherjee, W. Golletz, F. Sauvage, K. Giergiel, F. Mintert, and K. Sacha, Phase diagram and optimal control for n-tupling discrete time crystal, *New J. Phys.* **22**, 095001 (2020).
- [60] K. Giergiel, T. Tran, A. Zaheer, A. Singh, A. Sidorov, K. Sacha, and P. Hannaford, Creating big time crystals with ultracold atoms, *New J. Phys.* **22**, 085004 (2020).
- [61] T. Simula, Droplet time crystals, *Phys. Scr.* **98**, 035004 (2023).
- [62] L. Zou, D. Marcos, S. Diehl, S. Putz, J. Schmiedmayer, J. Majer, and P. Rabl, Implementation of the Dicke lattice model in hybrid quantum system arrays, *Phys. Rev. Lett.* **113**, 023603 (2014).
- [63] R. D. Jara Jr., D. F. Salinel, and J. G. Cosme, Theory of parametric resonance for discrete time crystals in fully connected spin-cavity systems, *Phys. Rev. A* **109**, 042212 (2024).
- [64] See Supplemental Material for further details on the validity of the AI approximation in periodically-driven systems, implementation of truncated Wigner approximation, and identification of KZM quantities and critical exponents.
- [65] B. Apffel and R. Fleury, Experimental observation of topological transition in linear and nonlinear parametric oscillators, *Phys. Rev. E* **109**, 054204 (2024).
- [66] R. D. Jara, P. Kongkhambut, H. Keßler, A. Hemmerich, and J. G. Cosme, Controlled bit flip of period-doubling and discrete time crystalline states in open systems, *Phys. Rev. B* **112**, 024303 (2025).
- [67] A. Polkovnikov, Phase space representation of quantum dynamics, *Ann. Phys.* **325**, 1790 (2010).
- [68] W. Chen, W. Lin, and Y. Zhu, Onset instability of a parametrically excited pendulum array, *Phys. Rev. E* **75**, 016606 (2007).
- [69] L. Mestre, S. Singh, G. Margiani, L. Catalini, A. Eichler, and V. Dumont, *A network of parametrically driven silicon nitride mechanical membranes* (2025), arXiv:2506.00850.
- [70] D. Iyama, T. Kamiya, S. Fujii, H. Mukai, Y. Zhou, T. Nagase, A. Tomonaga, R. Wang, J.-J. Xue, S. Watabe,

- S. Kwon, and J.-S. Tsai, Observation and manipulation of quantum interference in a superconducting Kerr parametric oscillator, *Nat Commun* **15**, 86 (2024).
- [71] D. H. White, S. Kato, N. Nemet, S. Parkins, and T. Aoki, Cavity dark mode of distant coupled atom-cavity systems, *Phys. Rev. Lett.* **122**, 253603 (2019).
- [72] R. Amsüss, C. Koller, T. Nöbauer, S. Putz, S. Rotter, K. Sandner, S. Schneider, M. Schramböck, G. Steinhäuser, H. Ritsch, J. Schmiedmayer, and J. Majer, Cavity QED with magnetically coupled collective spin states, *Phys. Rev. Lett.* **107**, 060502 (2011).
- [73] M. Scigliuzzo, G. Calajò, F. Ciccarello, D. Perez Lozano, A. Bengtsson, P. Scarlino, A. Wallraff, D. Chang, P. Delsing, and S. Gasparinetti, Controlling atom-photon bound states in an array of Josephson-junction resonators, *Phys. Rev. X* **12**, 031036 (2022).
- [74] T. Astner, S. Nevlacsil, N. Peterschofsky, A. Angerer, S. Rotter, S. Putz, J. Schmiedmayer, and J. Majer, Coherent coupling of remote spin ensembles via a cavity bus, *Phys. Rev. Lett.* **118**, 140502 (2017).
- [75] Y. Liu, J. You, and Q. Hou, Entanglement dynamics of Nitrogen-vacancy centers spin ensembles coupled to a superconducting resonator, *Sci Rep* **6**, 21775 (2016).

Supplemental Material for Kibble Zurek mechanism for dissipative discrete time crystal formation

Roy D. Jara Jr.¹ and Jayson G. Cosme¹

¹*National Institute of Physics, University of the Philippines, Diliman, Quezon City 1101, Philippines*

ADIABATIC-IMPULSE APPROXIMATION FOR PERIODICALLY-DRIVEN SYSTEMS

In this section, we derive an approximate analytic solution to the equations of motion of a dissipative linear parametric oscillator (DLPO) in the disordered state. We then use the results here to argue that the Adiabatic-Impulse (AI) approximation holds for any generic parametric oscillator. As such, if the system can be mapped onto a DLPO in the disordered phase, then it should satisfy the conditions for the AI approximation, and the KZM must hold for this system. Following this argument, we show that the Sine-Gordon model (SGM) and the Dicke lattice model (DLM) satisfy the condition for the AI approximation by mapping them onto a DLPO.

Dissipative linear parametric oscillator

Let us begin our analysis with the DLPO, which is given by Eq. (3) in the main text,

$$\ddot{\theta} + \gamma\dot{\theta} + \Omega^2 [1 + A \sin(\omega_d t)] \theta = 0. \quad (1)$$

To solve Eq. (1), we introduce a unitless timescale $\tilde{t} = \omega_d t$, and parameters $\mu = \gamma/\omega_d$, and $\Delta = \Omega/\omega_d$. Casting Eq. (1) in terms of these unitless quantities results in a dimensionless equation of motion

$$\frac{d^2}{d\tilde{t}^2} \theta + \mu \frac{d}{d\tilde{t}} \theta + \Delta^2 \theta + A \Delta^2 \sin(\tilde{t}) \theta = 0. \quad (2)$$

Suppose $A, \mu \ll 1$ such that the unitless dissipation can be parametrized by $A, \mu = A\Gamma$. We also consider the resonant case of $\omega_d = 2\Omega$, which then results to $\Delta^2 = 1/4$. To find an approximate solution for Eq. (2), we assume that the dynamics of θ has two timescales: a fast timescale, where the dynamics evolves at a timescale $\chi = \tilde{t}$; and a slow timescale, where the dynamics evolves at a timescale $\zeta = A\tilde{t}$, with $\chi \gg \zeta$ [1]. This assumption allows us to use the ansatz [1],

$$\theta(t) \approx \theta^{(0)}(\chi, \zeta) + A\theta^{(1)}(\chi, \zeta) + A^2\theta^{(2)}(\chi, \zeta) + \dots \quad (3)$$

Substituting Eq. (3) back to Eq. (2) and casting the equation of motion in terms of χ and ζ results to

$$\left(\frac{\partial^2 \theta^{(0)}}{\partial \chi^2} + \frac{1}{4} \theta^{(0)} \right) + A \left(\frac{\partial^2 \theta^{(1)}}{\partial \chi^2} + \frac{1}{4} \theta^{(1)} + 2 \frac{\partial^2 \theta^{(0)}}{\partial \chi \partial \zeta} + \Gamma \frac{\partial \theta^{(0)}}{\partial \chi} + \frac{1}{4} \sin(\chi) \theta^{(0)} \right) + \mathcal{O}(A^2) = 0. \quad (4)$$

Now, truncating Eq. (4) up to $\mathcal{O}(A)$, and imposing the equality, we see that the solution of $\theta^{(0)}$ takes the form,

$$\theta^{(0)} = \alpha(\zeta) e^{i\chi/2} + \alpha^*(\zeta) e^{-i\chi/2}. \quad (5)$$

If we substitute Eq. (5) back to Eq. (4), we also obtain the equations of motion for $\theta^{(1)}$,

$$\frac{\partial^2 \theta^{(1)}}{\partial \chi^2} + \frac{1}{4} \theta^{(1)} = -i \left(\frac{d\alpha}{d\zeta} + \frac{\Gamma}{2} \alpha - \frac{1}{8} \alpha^* \right) e^{i\chi/2} - \frac{i}{8} \alpha e^{i3\chi/2} + \text{cc}. \quad (6)$$

Notice that Eq. (6) takes the form of a linear oscillator that is driven both resonantly (first term) and off-resonantly (second term). In order for the ansatz in Eq. (3) to work, we have to impose the condition that $\theta^{(0)} \gg A\theta^{(1)}$, which only works if $\theta^{(1)}$ remains bounded. As such, we have to perform a secular approximation on Eq. (6), where we set all the resonant terms to zero [1]. This results in the slow-flow equation for the response amplitude of $\theta^{(0)}$,

$$\frac{d\alpha}{d\zeta} = -\frac{\Gamma}{2} \alpha + \frac{1}{8} \alpha^*. \quad \implies \quad \frac{d}{d\zeta} \begin{pmatrix} \alpha_R \\ \alpha_I \end{pmatrix} = \begin{pmatrix} -\frac{\Gamma}{2} + \frac{1}{8} & 0 \\ 0 & -\frac{\Gamma}{2} - \frac{1}{8} \end{pmatrix} \begin{pmatrix} \alpha_R \\ \alpha_I \end{pmatrix}, \quad (7)$$

where $\alpha = \alpha_R + i\alpha_I$. The response amplitude of $\theta^{(0)}$ is thus

$$\alpha(\zeta) = \alpha_{0,R} \exp\left[-\frac{1}{2}\left(\Gamma - \frac{1}{4}\right)\zeta\right] + i\alpha_{0,I} \exp\left[-\frac{1}{2}\left(\Gamma + \frac{1}{4}\right)\zeta\right], \quad (8)$$

where $\alpha_{0,R}$ and $\alpha_{0,I}$ are constants set by the initial values of the DLPO. In terms of t , Eq. (8) can be rewritten as

$$\alpha(t) = \alpha_{0,R} \exp\left[-\frac{1}{8}\left(\frac{4\gamma}{\omega_d} - A\right)\omega_d t\right] + i\alpha_{0,I} \exp\left[-\frac{1}{8}\left(\frac{4\gamma}{\omega_d} + A\right)\omega_d t\right]. \quad (9)$$

Given that $\omega_d = 2\Omega$, we can see that the real part of $\alpha(t)$ exponentially grows as soon as $A \geq 2\gamma/\Omega \equiv A_c$, resulting in the resonant state discussed in the main text. Below this driving amplitude, the system remains in a disordered state, where the initial value of α dictates the dynamics of the system. With all of this, the dynamics of θ up to the zeroth term is finally

$$\theta(t) \approx \left(\alpha_{0,R} e^{-\omega_d t/\tau_-} + i\alpha_{0,I} e^{-\omega_d t/\tau_+}\right) e^{-i\omega_d t/2} + \text{cc.}; \quad \tau_{\pm} = 8(A_c \pm A)^{-1}. \quad (10)$$

Now, let us discuss in full detail how Eq. (10) implies that the AI approximation must hold for the DLPO. Observe that near the critical point for $A < A_c$, the relaxation timescale of α_R , $\tau \equiv \tau_-$, diverges as we approach A_c . Meanwhile, the relaxation timescale of α_I , τ_+ , remains finite as $A \rightarrow A_c$. As such, α_I will decay faster than α_R near the critical point, allowing us to approximate the dynamics of θ near the critical point as

$$\theta(t) \approx \alpha_0 e^{-\omega_d t/\tau} e^{-i\omega_d t/2} + \text{cc.} \quad (11)$$

From this, we can readily see that the relaxation time of $\theta(t)$ diverges as $A \rightarrow A_c$, and thus the DLPO satisfies the condition of the AI approximation.

Sine-Gordon model

We now demonstrate that the SGM, described by the equation

$$\ddot{\theta}_\ell + \gamma\dot{\theta}_\ell + \Omega^2 [1 + A \sin(\omega_d t)] \sin \theta_\ell - g(\theta_{\ell+1} + \theta_{\ell-1} - 2\theta_\ell) = 0, \quad (12)$$

can be mapped onto a DLPO in the disordered phase. Here, we assume that $\tilde{T} = 0$ for simplicity. To do this, let us note that in the disordered phase, $\theta_\ell \approx 0$ and, thus, we can assume that $\sin \theta_\ell \approx \theta_\ell$. This results in an array of coupled DLPO of the form,

$$\ddot{\theta}_\ell + \gamma\dot{\theta}_\ell + \Omega^2 [1 + A \sin(\omega_d t)] \theta_\ell - g(\theta_{\ell+1} + \theta_{\ell-1} - 2\theta_\ell) = 0. \quad (13)$$

Using the discrete Fourier transform of θ_ℓ ,

$$\theta_\ell = \frac{1}{\sqrt{M}} \sum_k \theta_k e^{-ik\ell}, \quad (14)$$

where $k \in [-\pi, \pi)$, we can decouple Eq. (13), leading to the equation

$$\frac{1}{\sqrt{M}} \sum_k e^{ik\ell} \left\{ \ddot{\theta}_k + \gamma\dot{\theta}_k + [\Omega^2 (1 + A \sin(\omega_d t)) + 2g - 2g \cos k] \theta_k \right\} = 0, \quad (15)$$

which simplifies into

$$\ddot{\theta}_k + \gamma\dot{\theta}_k + \Omega_{\text{Res}}^2(k) \theta_k + \Omega^2 A \sin(\omega_d t) \theta_k = 0. \quad (16)$$

Here, $\Omega_{\text{Res}}^2(k) = \Omega^2 + 2g - 2g \cos(k)$ is the frequency band of the SGM, which is shown in Fig. 2(b) of the main text. Comparing Eq. (1) and Eq. (16), we can readily conclude that the SGM satisfies the condition for the AI approximation. Thus, the SGM can exhibit the main signatures of the KZM when transitioning to a classical DTC. Note that the form of Eq. (16) also reveals the mechanism behind the tunability of the spatial configuration of the classical DTCs in the SGM, which is the collective excitation of the system into a resonant state with a wave vector k when driven at a frequency $\omega_d = 2\Omega_{\text{Res}}(k)$. This is the same mechanism behind the Faraday waves in oscillating media [2].

Dicke lattice model

We next demonstrate that we can also map the DLM onto a DLPO. Consider the static Hamiltonian of the DLM,

$$\hat{H}/\hbar = \sum_{\ell}^M \left[\omega \hat{a}_{\ell}^{\dagger} \hat{a}_{\ell} + \omega_0 \hat{S}_{\ell}^z + \frac{2\lambda}{\sqrt{N}} \left(\hat{a}_{\ell}^{\dagger} + \hat{a}_{\ell} \right) \hat{S}_{\ell}^x - J \left(\hat{a}_{\ell+1}^{\dagger} \hat{a}_{\ell} + \hat{a}_{\ell}^{\dagger} \hat{a}_{\ell+1} \right) \right]. \quad (17)$$

To linearize Eq. (17), we employ a Holstein-Primakoff representation, where we map the collective spin operators onto bosonic operators via the mapping [3, 4]

$$\hat{S}_{\ell}^z = \hat{b}_{\ell}^{\dagger} \hat{b}_{\ell} - \frac{N}{2}, \quad \hat{S}_{\ell}^{-} = \left(\hat{S}_{\ell}^{+} \right)^{\dagger} = \sqrt{N} \sqrt{1 - \frac{\hat{b}_{\ell}^{\dagger} \hat{b}_{\ell}}{N}} \hat{b}_{\ell}. \quad (18)$$

For $\lambda < \lambda_c$, the system is in the normal phase, in which the spin excitation is negligible, i.e., $\langle \hat{b}_{\ell}^{\dagger} \hat{b}_{\ell} \rangle \ll N$. This allows us to expand the square-root operator in the \hat{S}_{ℓ}^{-} up to the zeroth order term, resulting in the mapping

$$\hat{S}_{\ell}^z = \hat{b}_{\ell}^{\dagger} \hat{b}_{\ell} - \frac{N}{2}, \quad \hat{S}_{\ell}^{-} = \sqrt{N} \sqrt{1 - \frac{\hat{b}_{\ell}^{\dagger} \hat{b}_{\ell}}{N}} \hat{b}_{\ell} \approx \left(1 - \frac{1}{2N} \hat{b}_{\ell}^{\dagger} \hat{b}_{\ell} + \dots \right) \sqrt{N} \hat{b}_{\ell} \approx \sqrt{N} \hat{b}_{\ell}. \quad (19)$$

Substituting Eq. (19) back to Eq. (17), noting that $2\hat{S}_{\ell}^x = \hat{S}_{\ell}^{-} + \hat{S}_{\ell}^{+}$, results to the quadratic Hamiltonian

$$\hat{H}/\hbar = \sum_{\ell}^M \left[\omega \hat{a}_{\ell}^{\dagger} \hat{a}_{\ell} + \omega_0 \hat{b}_{\ell}^{\dagger} \hat{b}_{\ell} + \lambda \left(\hat{a}_{\ell}^{\dagger} + \hat{a}_{\ell} \right) \left(\hat{b}_{\ell}^{\dagger} + \hat{b}_{\ell} \right) - J \left(\hat{a}_{\ell+1}^{\dagger} + \hat{a}_{\ell}^{\dagger} \hat{a}_{\ell+1} \right) \right], \quad (20)$$

up to a constant factor. We next decouple the bosonic modes \hat{a}_{ℓ} by moving to the momentum basis using the discrete Fourier transform of \hat{a}_{ℓ} and \hat{b}_{ℓ}

$$\hat{a}_{\ell} = \frac{1}{\sqrt{M}} \sum_k \hat{a}_k e^{-ik\ell}, \quad \hat{b}_{\ell} = \frac{1}{\sqrt{M}} \sum_k \hat{b}_k e^{-ik\ell}, \quad (21)$$

where $k \in [-\pi, \pi)$. Substituting Eq. (21) back to Eq. (20) results to a set of decoupled oscillators of the form

$$\hat{H}/\hbar = \sum_k \left[(\omega - 2J \cos k) \hat{a}_k^{\dagger} \hat{a}_k + \omega_0 \hat{b}_k^{\dagger} \hat{b}_k + \lambda \left(\hat{a}_k^{\dagger} \hat{b}_k + \hat{b}_k^{\dagger} \hat{a}_k \hat{a}_k \hat{b}_{-k} + \hat{a}_k^{\dagger} \hat{b}_{-k}^{\dagger} \right) \right]. \quad (22)$$

Finally, we incorporate the effects of dissipation in the system's polariton band structure by directly solving the Heisenberg equation

$$\frac{d}{dt} \langle \hat{A} \rangle = \left\langle i \left[\hat{H}/\hbar, \hat{A} \right] + \kappa \sum_k \left(2\hat{a}_k^{\dagger} \hat{A} \hat{a}_k - \left\{ \hat{a}_k^{\dagger} \hat{a}_k, \hat{A} \right\} \right) \right\rangle, \quad (23)$$

where $\hat{A} \in \left\{ \hat{a}_k, \hat{b}_k, \hat{a}_k^{\dagger}, \hat{b}_k^{\dagger} \right\}$. Doing this results in a set of coupled linear differential equations of the form

$$\frac{d}{dt} \begin{pmatrix} \langle \hat{a}_k \rangle \\ \langle \hat{b}_k \rangle \\ \langle \hat{a}_k^{\dagger} \rangle \\ \langle \hat{b}_k^{\dagger} \rangle \end{pmatrix} = \begin{pmatrix} -i\omega_0 & -i\lambda & 0 & -i\lambda \\ -i\lambda & -i\omega_k - \kappa & -i\lambda & 0 \\ 0 & i\lambda & i\omega_0 & i\lambda \\ i\lambda & 0 & i\lambda & i\omega_k - \kappa \end{pmatrix} \begin{pmatrix} \langle \hat{a}_k \rangle \\ \langle \hat{b}_k \rangle \\ \langle \hat{a}_k^{\dagger} \rangle \\ \langle \hat{b}_k^{\dagger} \rangle \end{pmatrix} = \mathbb{M} \begin{pmatrix} \langle \hat{a}_k \rangle \\ \langle \hat{b}_k \rangle \\ \langle \hat{a}_k^{\dagger} \rangle \\ \langle \hat{b}_k^{\dagger} \rangle \end{pmatrix}, \quad (24)$$

where $\omega_k = \omega - 2J \cos k$. In the basis in which \mathbb{M} is diagonal, we can effectively describe the DLM as a set of decoupled oscillators corresponding to the lower and upper polariton bands with frequencies $\Omega_{\text{res,LP}}(k) \equiv \text{Im}[\Lambda_{\text{LP}}(k)]$ and $\Omega_{\text{res,UP}}(k) \equiv \text{Im}[\Lambda_{\text{UP}}(k)]$, where $\Lambda_{\text{LP,UP}}$ are the eigenvalues of \mathbb{M} . Each polariton band experiences an effective dissipation set by $\text{Re}[\Lambda_{\text{LP,UP}}]$. As such, if we periodically drive the polariton modes at a driving amplitude $A \ll 1$, we can effectively describe the DLM as a DLPO.

TRUNCATED WIGNER APPROXIMATION FOR THE DICKE LATTICE MODEL

Consider the master equation of the Dicke lattice model shown in the main text,

$$\frac{d}{dt}\hat{\rho} = i \left[\hat{H}/\hbar, \hat{\rho} \right] + \kappa \sum_{\ell=1}^M \left(2\hat{a}_{\ell}\hat{\rho}\hat{a}_{\ell}^{\dagger} - \left\{ \hat{a}_{\ell}^{\dagger}\hat{a}_{\ell}, \hat{\rho} \right\} \right). \quad (25)$$

As mentioned, while we can compute the full density matrix $\hat{\rho}$ to obtain the quantum dynamics of the system, this method is computationally expensive since the Hilbert space grows exponentially with the system size. We circumvent this problem by employing the truncated Wigner approximation (TWA) as follows. We begin by approximating the equations of motion of the system using the Heisenberg-Langevin equation [5],

$$\frac{d}{dt}\hat{a}_{\ell} = i \left[\hat{H}/\hbar, \hat{a}_{\ell} \right] - \kappa\hat{a}_{\ell} + \hat{\Xi}_{\ell}(t), \quad \frac{d}{dt}\hat{S}_{\ell}^{x,y,z} = i \left[\hat{H}/\hbar, \hat{S}_{\ell}^{x,y,z} \right]. \quad (26)$$

This approximation is typically employed in simulations for atom-cavity systems, where the system size is typically of orders $N \gtrsim 10^4$ [5]. Here, $\hat{\Xi}_{\ell}(t)$ is a Gaussian noise operator satisfying the relations $\langle \hat{\Xi}_{\ell}(t) \rangle = 0$ and $\langle \hat{\Xi}_{\ell}(t)\hat{\Xi}_{\ell'}(t') \rangle = \kappa\delta(t-t')\delta_{\ell,\ell'}$. After evaluating the commutation relations between \hat{H} , \hat{a}_{ℓ} and $\hat{S}_{\ell}^{x,y,z}$, we approximate the system's dynamics by replacing the operators with complex variables, with $\hat{a}_{\ell}, \hat{\Xi}_{\ell}(t) \rightarrow a_{\ell}, \Xi_{\ell}(t) \in \mathbb{C}$ and $\hat{S}_{\ell}^{x,y,z} \rightarrow S_{\ell}^{x,y,z}$. Doing this results in a set of stochastic differential equations of the form,

$$da_{\ell}^{\text{R}} = \left[\omega a_{\ell}^{\text{I}} - J(a_{\ell-1}^{\text{I}} + a_{\ell+1}^{\text{I}}) - \kappa a_{\ell}^{\text{R}} \right] dt + \sqrt{\frac{\kappa}{2}} dW_1, \quad (27a)$$

$$da_{\ell}^{\text{I}} = - \left[\omega a_{\ell}^{\text{R}} + \frac{2\lambda}{\sqrt{N}} S_{\ell}^x - J(a_{\ell-1}^{\text{R}} + a_{\ell+1}^{\text{R}}) + \kappa a_{\ell}^{\text{I}} \right] dt + \sqrt{\frac{\kappa}{2}} dW_2, \quad (27b)$$

$$\frac{d}{dt}S_{\ell}^x = -\omega_0 S_{\ell}^y, \quad \frac{d}{dt}S_{\ell}^y = \omega_0 S_{\ell}^x - \frac{4\lambda}{\sqrt{N}} a_{\ell}^{\text{R}} S_{\ell}^z, \quad \frac{d}{dt}S_{\ell}^z = \frac{4\lambda}{\sqrt{N}} a_{\ell}^{\text{R}} S_{\ell}^y, \quad (27c)$$

where $a_{\ell} = a_{\ell}^{\text{R}} + ia_{\ell}^{\text{I}}$. Here, W_i is the Wiener process satisfying the condition $\langle dW_i \rangle = 0$ and $\langle dW_i dW_j \rangle = \delta_{i,j} dt$ for $i \in \{1, 2\}$.

The crux of the TWA lies in the sampling of multiple trajectories with different initial values and noise realizations to obtain the expectation value of the quantity of interest [6]. For the DLM, we consider an initial state in which the bosonic mode is in the vacuum state. This state can be numerically represented as a complex Gaussian number $a_{\ell}(t_i) = (\eta_{\ell}^{\text{R}} + i\eta_{\ell}^{\text{I}})/2$, where $\eta_{\ell}^{\text{R,I}}$ satisfies the condition $\langle \eta_{\ell}^i \rangle = 0$ and $\langle \eta_{\ell}^i \eta_{\ell'}^j \rangle = \delta_{\ell,\ell'} \delta_{i,j}$ for $i, j \in \{\text{R, I}\}$ [7]. Meanwhile, we consider a perturbed initial state of $\hat{S}_{\ell}^x = \epsilon N/2$, $\hat{S}_{\ell}^y = 0$, and $\hat{S}_{\ell}^z = -N\sqrt{1-\epsilon^2}/2$, with $\epsilon = 10^{-6}$, for the collective spins at each sites. Solving Eq. (27) for different initial bosonic mode configuration allows us to obtain a distribution for the transition delay \hat{t} and defect number n_d , which we can then use to calculate the $\langle \hat{t} \rangle$ and $\langle n_d \rangle$ shown in the main text.

IDENTIFICATION OF KZM QUANTITIES FOR DTC FORMATION

In this section, we provide a detailed explanation on how the transition time t_p , critical time t_c , and n_d are inferred from the individual trajectories of the SGM and the DLM. We also provide a discussion on how we obtain the correlation length at the transition time, $\xi(t_p)$, for both systems and how $\xi(t_p)$ scales with the quench time τ_q . In particular, we demonstrate that $\xi(t_p)$ indeed sets the steady-state n_d of the two systems, thus strengthening our argument that the KZM is responsible for the proliferation of spatial defects in DTCs.

Transition delay and defect number

We have discussed in the main text a recipe for obtaining the transition time t_p , the critical time t_c , and the defect number using the complex amplitude of a local order parameter O_{ℓ} . We now expand on this by showing an exemplary dynamics of the complex amplitude given some arbitrary DTC configuration. We present in Fig. 1(a) and 1(b) an exemplary dynamics of the DLM for the FM-DTC and AFM-DTC, respectively. Note that the dynamics of the $\text{Re}(a_{\ell}/\sqrt{N})$ is qualitatively similar to the

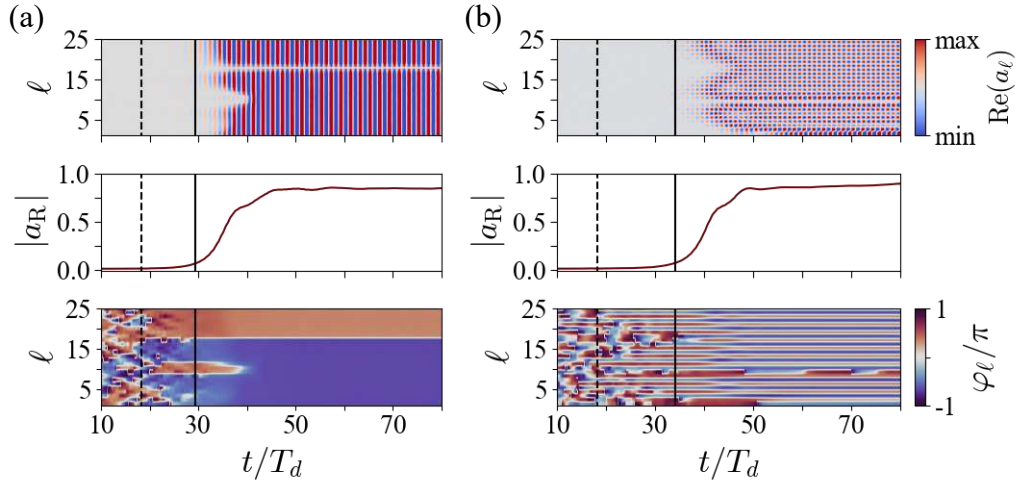


FIG. 1. (a)–(b) Single trajectory dynamics of the DLM for (a) FM-DTC and (b) AFM-DTC. The top panels show the real component of a_ℓ . The middle panels show the site average of $|a_{\ell,R}|/\sqrt{N}$, $|a_R|$, and the bottom panels show the spatiotemporal dynamics of φ_ℓ . The dashed lines mark the critical time t_c , while the solid lines mark the transition time t_p . The parameters used here are the same as the parameters for Fig. 4(c) and 4(d) in the main text.

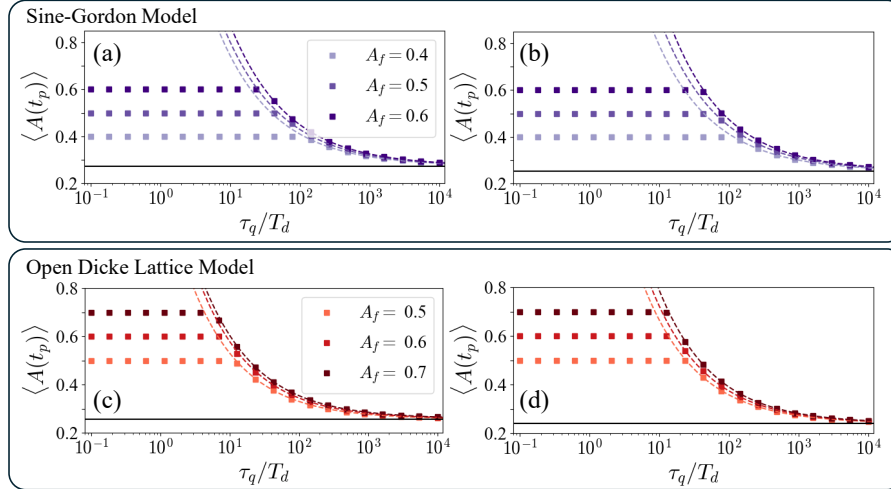


FIG. 2. (a)–(b) Ensemble average of the driving amplitude at the transition time t_p of the SGM for (a) the FM-DTC and (b) the AFM-DTC. The same parameters used in Fig. 3(a) and 3(b) are used to construct (a) and (b), respectively. (c)–(d) Average $A(t_p)$ for the (c) FM-DTC and (d) AFM-DTC of the DLM, with the parameters used in Figs. 5(a) and Figs. 5(b) of the main text, respectively.

dynamics of θ_ℓ for the SGM. As shown in the middle panels of Fig. 1, we can obtain the t_p by using a threshold criterion, in which we consider the system to be in a DTC if $|O_R(t)| \geq \delta \max\{|O_R(t)\}$, where $|O_R| = \sum_\ell |O_{\ell,R}|/M$, with $O_{\ell,R}$ being the complex amplitude of the local order parameter O_ℓ . In the case of the DLM, $O_\ell = a_\ell/\sqrt{N}$ and $|O_R| = |a_R|$. As shown in the bottom panels of Fig. 1, the threshold $\delta = 0.15$ is enough to identify the time at which φ_ℓ has attained sufficient spatial long-range order to indicate that the system has formed a DTC. As for identifying the steady-state n_d , we simply obtain the value of φ_ℓ at the final simulation time t_f . In the case of the AFM-DTC, we also apply the transformation $\varphi_\ell^s = \varphi_\ell + [1 - (-1)^\ell] \pi/2$, with the condition $\varphi_\ell^s \in [-\pi, \pi)$, to separate the two symmetry-broken states associated with the antiferromagnetic ordering.

We identify t_c by doing the following. We first obtain the driving amplitude at the transition time, $A(t_p)$, for every single trajectory, and identify the scaling of its average, $\langle A(t_p) \rangle$, as a function of τ_q . We show the scaling of $\langle A(t_p) \rangle$ for the FM-DTC and AFM-DTC of the SGM in Figs. 2(a) and 2(b), respectively. We then show in Figs. 2(c) and 2(d) the same scaling for the FM-DTC and AFM-DTC of the DLM, respectively. Note that the interval of τ_q in which $\langle A(t_p) \rangle$ remains constant corresponds to the regime where the KZM breaks down. Meanwhile, the interval of τ_q in which $\langle A(t_p) \rangle$ follows a power-law behavior corresponds to the regime where the KZM is valid. We then obtain the critical point by fitting the function $A(\tau_q) = a\tau_q^{-b} + c$ to the data

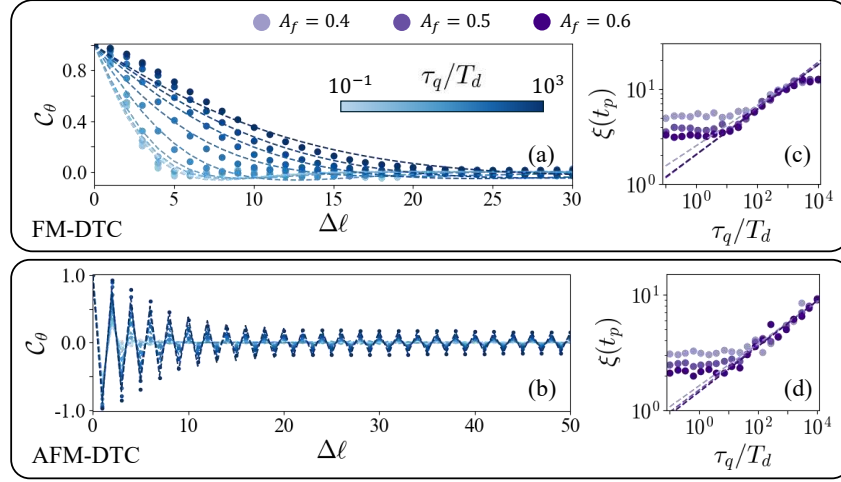


FIG. 3. (a)–(b) Exemplary site correlation C_θ of the SGM for the (a) FM-DTC and (b) the AFM-DTC as a function of the quench time τ_q . (c)–(d) Correlation length of the SGM as a function of τ_q and A_f for (a) the FM-DTC and (b) the AFM-DTC. The parameters used are the same as the parameters used in Fig. 3 of the main text.

points. This is justified by how in the KZM regime, it is predicted that $\varepsilon(t_p) = [A(t_p) - A_c]/A_c = (A_0/A_c)\tau_q^{-1/(1+\nu z)}$, where A_0 is a proportionality constant [8]. Rewriting the scaling of $\varepsilon(t_p)$ as $A(t_p) = A_0\tau_q^{-1/(1+\nu z)} + A_c$ makes it apparent that the fitting parameters a and b corresponds to the scaling coefficients and exponents of $\varepsilon(t_p)$, respectively, while the fitting parameter c corresponds to the critical point. We show the extrapolated critical points for the SGM and the DLM as solid horizontal lines in Fig. 2. Finally, we obtain t_c using the equation $t_c = (A_c - A_i)\tau_q/(A_f - A_i)$.

Correlation length at transition time

Another quantity that can be used to establish the presence of KZM in DTCs is the correlation length at t_p , $\xi(t_p)$, which we calculate as follows. We again consider an arbitrary order parameter O_ℓ and its complex amplitude $O_{\ell,R}$. The spatial correlation of $O_{\ell,R}$ at t_p is defined as

$$C_O = \frac{\sum_\ell \langle O_{\ell+\Delta\ell,R}^*(t_p) O_{\ell,R}(t_p) + O_{\ell,R}^*(t_p) O_{\ell+\Delta\ell,R}(t_p) \rangle}{2 \sum_\ell \langle |O_{\ell,R}(t_p)|^2 \rangle}, \quad (28)$$

where $\langle \dots \rangle$ denotes an ensemble average over multiple trajectories. We present in Figs. 3(a) and 3(b) the calculated spatial correlation of the SGM for the FM-DTC and AFM-DTC, respectively, with $O_\ell = \theta_\ell$. Notice that for the FM-DTC, C_θ follows an approximate exponential behavior with a long-wavelength modulation. This motivates us to use the fitting function $C_\theta = e^{-\Delta\ell/a} \cos(b\Delta\ell)$, where a corresponds to the correlation length, while b corresponds to the frequency of C_θ . As for the AFM-DTC, C_θ oscillates between a positive and negative value at each site, while exponentially decaying towards a finite value. This behavior is a characteristic of anti-ferromagnetic ordering. Due to the finite value of C_θ at large $\Delta\ell$ for the AFM-DTC, we use the fitting function $C_\theta = [e^{-\Delta\ell/a} + c(1 - e^{-\Delta\ell/a})] \cos(b\Delta\ell)$ instead, where c is the extrapolated saturation value of C_θ . Note that for $c = 0$, we recover the fitting function for the FM-DTC. We present in Figs. 3(c) and 3(d) the extrapolated $\xi(t_p)$ as a function of τ_q for the FM-DTC and AFM-DTC of the SGM, respectively. Notably, we see a power-law scaling for both DTC configurations at $\tau_q/T_d \geq 10^2$, which is a signature of the KZM. This behavior is consistent with the behavior observed with \hat{t} and n_d as shown in the main text.

We also calculate the spatial correlation of the DLM for $O_\ell = a_\ell$, as shown in Figs. 4(a) and 4(b) for the FM-DTC and AFM-DTC, respectively. Notably, the behavior of C_a is consistent with the behavior of C_θ , allowing us to use the same fitting functions to obtain $\xi(t_p)$. We present in Figs. 4(c) and 4(d) the scaling of $\xi(t_p)$ as a function of τ_q for the FM-DTC and AFM-DTC of the DLM, respectively. Similar to the SGM, we observe a power-law scaling for $\tau_q/T_d \geq 10^1$, which is a signature of the KZM. This is consistent with the results discussed in the main text.

Now that we have established the power-law scaling of $\xi(t_p)$ for both systems, we now demonstrate that the correlation at t_p is responsible for setting the n_d in the long-time behavior of the DTCs. To do this, we note that in the KZM regime, $|\varepsilon(t_p)| \propto \tau_q^{-1/(1+\nu z)}$, which then implies that $\xi(t_p) \propto |\varepsilon(t_p)|^{-\nu} \propto \tau_q^{\nu/(1+\nu z)} = \tau_q^{\beta_\xi}$ [8]. Given that $n_d \propto \tau_q^{-(D-d)\nu/(1+\nu z)} = \tau_q^{-\beta_{n_d}}$, we

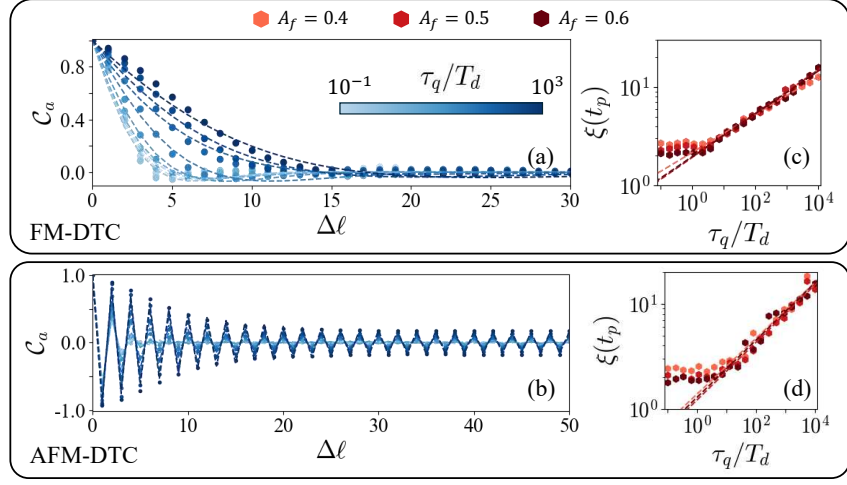


FIG. 4. (a)–(b) Exemplary site correlation C_θ of the DLM for (a) the FM-DTC and (b) the AFM-DTC as a function of the quench time τ_q . (c)–(d) Correlation length of the DLM as a function of τ_q and A_f for (a) the FM-DTC and (b) the AFM-DTC. The parameters used are the same as the parameters used in Fig. 5 of the main text.

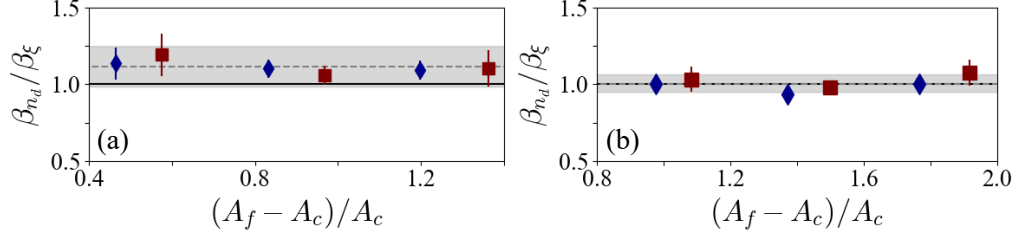


FIG. 5. (a)–(b) Ratio of the scaling exponents of n_d and $\xi(t_p)$ of (a) the SGM and (b) the DLM for different DTC configurations and A_f . The solid lines mark $\beta_{n_d}/\beta_\xi = 1$ for a one-dimensional system with point defects. The dashed lines mark the value of β_{n_d}/β_ξ averaged over different A_f , while the shaded region corresponds to the standard deviation of β_{n_d}/β_ξ .

should expect that if $\xi(t_p)$ sets the n_d , then the ratio of their scaling exponents must satisfy the relations $\beta_{n_d}/\beta_\xi = D - d$, where D is the system dimension, and d is defect dimension. This condition is independent of the details of the system and the ramp. We verify that the SGM and DLM satisfy this condition in Figs. 5(a) and 5(b), respectively. In particular, for both systems, the theoretical value $\beta_{n_d}/\beta_\xi = 1$ for one-dimensional systems with point defects lies within the one standard deviation of β_{n_d}/β_ξ averaged over different A_f . These results strengthen our claim that it is the KZM that is responsible for the proliferation of defects in DTCs for large quench times.

UNIVERSALITY AND CRITICAL EXPONENTS

Let us now address the universality of the KZM observed for the DTCs. Consider again our arguments for the validity of AI approximation in periodically driven systems. We have demonstrated that near the critical point of the DLPO, the relaxation time follows the scaling $\tau \propto \varepsilon^{-1}$, where $\varepsilon = (A_f - A_c)/A_c$. If we assume that the proportionality $\tau \propto |\varepsilon|^{-vz}$ also holds for the DLPO, then it follows that $vz = 1$ for the DLPO. This implies that any system transitioning towards a DTC must satisfy the scaling $\hat{t} \propto \tau_q^{vz/(1+vz)} = \tau_q^{\beta_{\hat{t}}}$, with $\beta_{\hat{t}} = 1/2$ regardless of the details of the system, so long as the system can be mapped onto a DLPO. We verify this in Fig. 6(a), where we compare the scaling exponent of $\langle \hat{t} \rangle$ for the SGM and DLM for different DTC configurations. Notably, our results agree well with the predicted scaling exponent for \hat{t} , establishing the universality of our results across different systems.

While we expect vz to be universal, the static and dynamic critical exponents, v and z , respectively, can still vary between systems. For instance, as shown in Fig. 6(b), the critical exponents of the SGM transitioning to either FM-DTC or AFM-DTC are close to the mean-field critical exponents $v = 0.5$ and $z = 2$ [8]. Meanwhile, as shown in Fig. 6(c), the critical exponents of the DLM deviate from the mean-field critical exponents. In particular, while both DTC configurations have $v \approx 0.5$, the

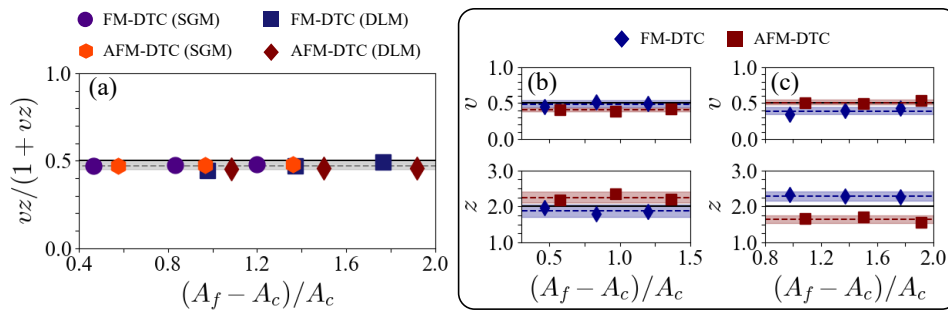


FIG. 6. (a) Scaling exponent of $\langle \hat{t} \rangle$ for different system and DTC configuration. The solid line marks the predicted scaling exponent of \hat{t} for $vz = 1$. (b)–(c) Critical exponents of (b) the SGM and (c) DLM for different DTC configurations. The top panels show the static critical exponent v , while the bottom panels show the dynamic critical exponent z . The solid lines mark the values of v and z for the mean-field universality class. The dashed lines correspond to the v and z averaged across different A_f , while the shaded regions correspond to the standard deviation associated with the average v and z .

FM-DTC has a larger z than the AFM-DTC, with $z \approx 2.25$. Meanwhile, the AFM-DTC has the dynamical critical exponent of $z \approx 1.75$. Note that in calculating v and z , we have used the relations

$$v = \frac{\beta_{n_d}}{1 - \beta_{\hat{t}}}, \quad z = \frac{\beta_{\hat{t}}}{\beta_{n_d}}, \quad (29)$$

where $\beta_{\hat{t}}$ and β_{n_d} are the magnitude of the scaling exponents of $\langle \hat{t} \rangle$ and $\langle n_d \rangle$, respectively. It will be interesting to know the mechanism behind the deviation between the critical exponents of the DTC-forming SGM and DLM, and to determine whether system-specific details such as dissipation and geometry affect these critical exponents.

-
- [1] I. Kovacic, R. Rand, and S. M. Sah, Mathieu's equation and its generalizations: Overview of stability charts and their features, *Appl. Mech. Rev.* **70**, 020802 (2018).
- [2] J. Miles and D. Henderson, Parametrically forced surface waves, *Annu. Rev. Fluid Mech.* **22**, 143 (1990).
- [3] C. Emary and T. Brandes, Chaos and the quantum phase transition in the Dicke model, *Phys. Rev. E* **67**, 066203 (2003).
- [4] R. D. Jara Jr. and J. G. Cosme, Apparent delay of the Kibble-Zurek mechanism in quenched open systems, *Phys. Rev. B* **110**, 064317 (2024).
- [5] H. Ritsch, P. Domokos, F. Brennecke, and T. Esslinger, Cold atoms in cavity-generated dynamical optical potentials, *Rev. Mod. Phys.* **85**, 553 (2013).
- [6] A. Polkovnikov, Phase space representation of quantum dynamics, *Ann. Phys.* **325**, 1790 (2010).
- [7] M. K. Olsen and A. S. Bradley, Numerical representation of quantum states in the positive-P and Wigner representations, *Opt. Commun.* **282**, 3924 (2009).
- [8] A. del Campo and W. H. Zurek, Universality of phase transition dynamics: Topological defects from symmetry breaking, *Int. J. Mod. Phys. A* **29**, 1430018 (2014).